

An ultrafast symmetry switch in a Weyl semimetal

Edbert J. Sie^{1,2,13}, Clara M. Nyby^{3,13}, C. D. Pemmaraju², Su Ji Park², Xiaozhe Shen⁴, Jie Yang^{4,5}, Matthias C. Hoffmann⁴, B. K. Ofori-Okai^{4,6}, Renkai Li⁴, Alexander H. Reid⁴, Stephen Weathersby⁴, Ehren Mannebach⁷, Nathan Finney⁸, Daniel Rhodes^{9,10,12}, Daniel Chenet⁸, Abhinandan Antony⁸, Luis Balicas^{9,10}, James Hone⁸, Thomas P. Devereaux^{1,2}, Tony F. Heinz^{2,5,11}, Xijie Wang⁴ & Aaron M. Lindenberg^{2,5,7*}

Topological quantum materials exhibit fascinating properties^{1–3}, with important applications for dissipationless electronics and fault-tolerant quantum computers^{4,5}. Manipulating the topological invariants in these materials would allow the development of topological switching applications analogous to switching of transistors⁶. Lattice strain provides the most natural means of tuning these topological invariants because it directly modifies the electron–ion interactions and potentially alters the underlying crystalline symmetry on which the topological properties depend^{7–9}. However, conventional means of applying strain through heteroepitaxial lattice mismatch¹⁰ and dislocations¹¹ are not extendable to controllable time-varying protocols, which are required in transistors. Integration into a functional device requires the ability to go beyond the robust, topologically protected properties of materials and to manipulate the topology at high speeds. Here we use crystallographic measurements by relativistic electron diffraction to demonstrate that terahertz light pulses can be used to induce terahertz-frequency interlayer shear strain with large strain amplitude in the Weyl semimetal WTe₂, leading to a topologically distinct metastable phase. Separate nonlinear optical measurements indicate that this transition is associated with a symmetry change to a centrosymmetric, topologically trivial phase. We further show that such shear strain provides an ultrafast, energy-efficient way of inducing robust, well separated Weyl points or of annihilating all Weyl points of opposite chirality. This work demonstrates possibilities for ultrafast manipulation of the topological properties of solids and for the development of a topological switch operating at terahertz frequencies.

Topological materials provide a platform from which to pursue exotic physics from the seemingly distant field of particle physics in condensed matter systems, such as Weyl fermions^{12–14}. This has led to a worldwide effort focused on discovering new topological quantum materials. One prime example is WTe₂, which is a layered transition-metal dichalcogenide (TMD) that crystallizes in a distorted hexagonal net with an orthorhombic unit cell, where the W–W chain direction is along the crystallographic axis *a* (Fig. 1a)¹⁵. The lack of inversion symmetry in this material leads to a topological semimetal (predicted¹⁶ and experimentally verified^{17–19}) with type II Weyl points (WPs), which can be manipulated through atomic-scale lattice distortions. In our experiments, the measured shear displacement amplitudes (about 1%) are more than sufficient to undergo a complete annihilation of the WPs or a more-than-twofold increase in WP separation, depending on the direction of the shear displacement. Ordinary crystals start to fracture at these strains, and conventional means of using piezoelectric transducers to induce lattice distortions typically reach about 0.05% strain²⁰. The observed large strain in our experiment (about 1%) is possible because we use light to generate interlayer shear strain in a

weakly van-der-Waals-bonded two-dimensional TMD—a method that is less susceptible to lattice damage than uniaxial straining but that can considerably alter the electronic band structure.

We used a relativistic ultrafast electron diffraction (UED) technique to reconstruct the shear motion and crystallographically quantify the corresponding atomic displacements by measuring more than 200 Bragg peaks (Fig. 1b)²¹ (Methods). We used two different terahertz pump excitation schemes, involving a quasi-single-cycle excitation at 3 THz and a few-cycle excitation at 23 THz, both of which enable application of an all-optical bias field while minimizing interband transitions (Methods). The arrival time of the electron beam (probe) can be adjusted with respect to the terahertz pulses (pump) using an optical delay stage. The measured diffraction pattern in equilibrium (Fig. 1c) is consistent with the orthorhombic phase of WTe₂ (Fig. 1a). By applying terahertz pump pulses, we find that the intensities of many Bragg peaks are modulated, which indicates structural changes in the WTe₂ lattice. To investigate the lattice dynamics, we plot the intensity changes $\Delta I/I_0$ of several Bragg peaks as a function of the time delay, Δt , between the terahertz pump and electron probe pulses (Fig. 1d, e). The time traces show coherent oscillations with a frequency of 0.24 THz (Fig. 1f), which is consistent with a low-frequency interlayer shear phonon mode predicted by density functional theory (DFT) analysis (Methods).

To determine the atomic motion, we plot the measured $\Delta I/I_0$ image at 2.5 ps (Fig. 2a). We find that the changes in peak intensity alternate along the *b* axis, while peaks (*hkl*) with *k* = 0 show negligible changes. This suggests that the interlayer shear displacement is along the *b* axis. To verify this, we derive the peak intensity modulation $\Delta I/I_0$ by introducing a top-layer shear displacement Δy with respect to the bottom layer into the structure factor

$$S(\Delta y) = 2 \sum_{\text{top}} f_j \cos[2\pi(hx_j + ky_j) + \pi k \Delta y] \quad (1)$$

where we have used the underlying crystalline symmetry in WTe₂ to obtain the final, simplified expression (Methods). Here, the summation runs over all atoms in the top half of the unit cell (two W and four Te atoms), f_j is the atomic scattering factor, $(x_j, \hat{a}, y_j, \hat{b}, z_j, \hat{c})$ is the atom position in the unit cell, *hkl* are the usual Miller indices for the [001] zone axis, and the lattice constants are *a* = 3.477 Å, *b* = 6.249 Å and *c* = 14.018 Å. To compare this with our experiment, we calculate the peak intensity modulation $\Delta I \propto |S(\Delta y)|^2 - |S(0)|^2$, shown in Fig. 2b. Here, we define a positive shear displacement ($\Delta y > 0$), as shown in the inset of Fig. 2e. The simulated image shows excellent agreement with the measured image and verifies that the peak intensity modulation arises primarily from interlayer shear displacement along the *b* axis.

We determine the shear displacement amplitude through a global fitting between the simulated and measured intensities of many Bragg

¹Geballe Laboratory for Advanced Materials, Stanford University, Stanford, CA, USA. ²SIMES, SLAC National Accelerator Laboratory, Menlo Park, CA, USA. ³Department of Chemistry, Stanford University, Stanford, CA, USA. ⁴SLAC National Accelerator Laboratory, Menlo Park, CA, USA. ⁵PULSE Institute, SLAC National Accelerator Laboratory, Menlo Park, CA, USA. ⁶Department of Chemistry, Massachusetts Institute of Technology, Cambridge, MA, USA. ⁷Department of Materials Science and Engineering, Stanford University, Stanford, CA, USA. ⁸Department of Mechanical Engineering, Columbia University, New York, NY, USA. ⁹National High Magnetic Field Laboratory, Florida State University, Tallahassee, FL, USA. ¹⁰Department of Physics, Florida State University, Tallahassee, FL, USA. ¹¹Department of Applied Physics, Stanford University, Stanford, CA, USA. ¹²Present address: Department of Mechanical Engineering, Columbia University, New York, NY, USA. ¹³These authors contributed equally: Edbert J. Sie, Clara M. Nyby. *e-mail: aaronl@stanford.edu

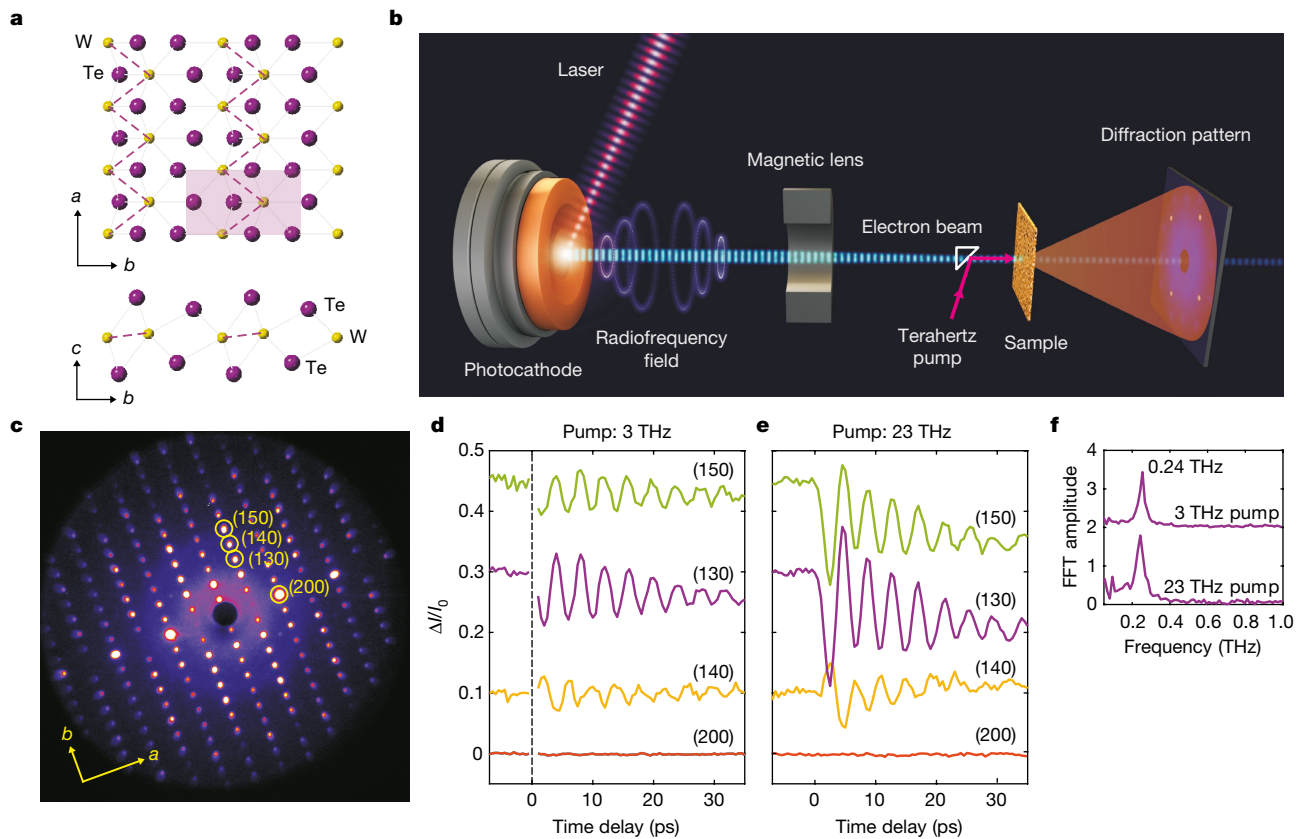


Fig. 1 | Observation of coherent interlayer shear displacements in WTe_2 measured using relativistic ultrafast electron diffraction. **a**, Lattice structure of Td WTe_2 : top view (a - b plane) and side view (b - c plane). The dashed lines indicate the W-W zigzag chain along the a axis. The shaded area shows the unit cell. **b**, Schematic of SLAC 3-MeV relativistic ultrafast electron diffraction setup. Image courtesy of G. Stewart. The electron beam is generated using ultraviolet femtosecond laser pulses at the photocathode and accelerated using an intense radiofrequency field from the klystron. The diffracted electron beam, measured using an EMCCD

(electron-multiplying charge-coupled device) camera, is used to probe the structural changes of the sample. Intense terahertz pump pulses are used to induce interlayer shear strain in WTe_2 . **c**, Measured diffraction pattern of WTe_2 at equilibrium. **d**, **e**, Changes in Bragg peak intensity as a function of time delay between the terahertz pump pulses and the electron beam. **f**, Fast Fourier transform (FFT) amplitude of the oscillations, indicating the 0.24-THz shear phonon mode along the b axis. Curves in **d**-**f** are offset for clarity.

peaks as a function of time delay (Methods). The fitting results (Fig. 2c, d) show that the proposed interlayer shear displacement fits the experimental data very well. At a low pump field of 2.6 MV cm^{-1} (23 THz), the fitting results (Fig. 2f; red line) show shear displacements that oscillate between -1.7 to $+3.6$ pm in the early stage and gradually develop an offset towards a positive shear displacement of $+1.5$ pm in the later stage. Increasing the pump field to 7.5 MV cm^{-1} (Fig. 2f; blue line) leads to a much larger offset of $+8.0$ pm (1.3% strain) that gradually builds up on a timescale of 25 ps and persists for longer than 70 ps. This long-lived offset indicates that the lattice has found a new equilibrium position, deviating from the simple harmonic oscillator behaviour that is normally expected. The shear oscillation frequency decreases at increasing field strengths (Extended Data Fig. 6), consistent with an anharmonic response as the material is driven to large amplitudes.

To investigate the driving mechanism of this behaviour, we measured the shear amplitude as a function of pump field strength and polarization. We found that the amplitude increases linearly with the field under different off-resonance frequencies (Fig. 3a) and is polarization-isotropic (Fig. 3b, c). Moreover, the shear motion always starts towards positive displacement regardless of polarization (Fig. 3b). This behaviour cannot be explained through the infrared active and Raman (impulsive stimulated Raman scattering) mechanisms normally considered. We propose a terahertz-field-driven charge-current mechanism, as indicated by the linear amplitude response to field strength and motivated by recent calculations²² that predict a transition from an orthorhombic (Td) to a monoclinic and centrosymmetric ($1T'$) phase in WTe_2 via hole doping at a density of about 10^{20} cm^{-3} . Microscopically,

the applied field accelerates the electron population away from the top-most valence band, which constitutes an interlayer antibonding orbital. This destabilizes the interlayer coupling strength and launches a shear motion along the in-plane transition pathway from the Td to the $1T'$ phase with a new equilibrium position ($\Delta y > 0$) (Fig. 2e, Extended Data Fig. 1). In our experiment, the effective hole doping density can be estimated using the Drude model, which gives a doping density of about 10^{20} cm^{-3} , comparable to the impulsive driving force for the interlayer shear motion (Methods).

We note that a departure from the Td phase via interlayer displacement could result in two possible phases, monoclinic $1T'$ and orthorhombic $1T'(*)$, both of which are centrosymmetric. Unlike the $1T'$ phase, the $1T'(*)$ phase can be reached while maintaining the orthorhombic structure (Extended Data Fig. 1). Although the observed long-lived offset (8 pm; Fig. 2f) is somewhat smaller than that calculated for a complete transition to the $1T'(*)$ phase (about 10–15 pm; Fig. 2e), the measured displacement should be viewed as a lower bound due to spatial averaging of the film seen by the electron beam. This is because under the simplistic approximation that the induced metastable phase is a centrosymmetric phase, either $1T'(*)$ or $1T'$, the volume change associated with this transformation results in a complex longitudinally heterogeneous strain profile with strain waves propagating from the interfaces²³ and complicated by substrate interactions. These processes probably underlie some of the complex longer-timescale dynamics (of the order of 25 ps) shown in Fig. 2f. This timescale is consistent with the shear-wave propagation time across the sample thickness (Methods; Extended Data Fig. 4), which is longer than recently

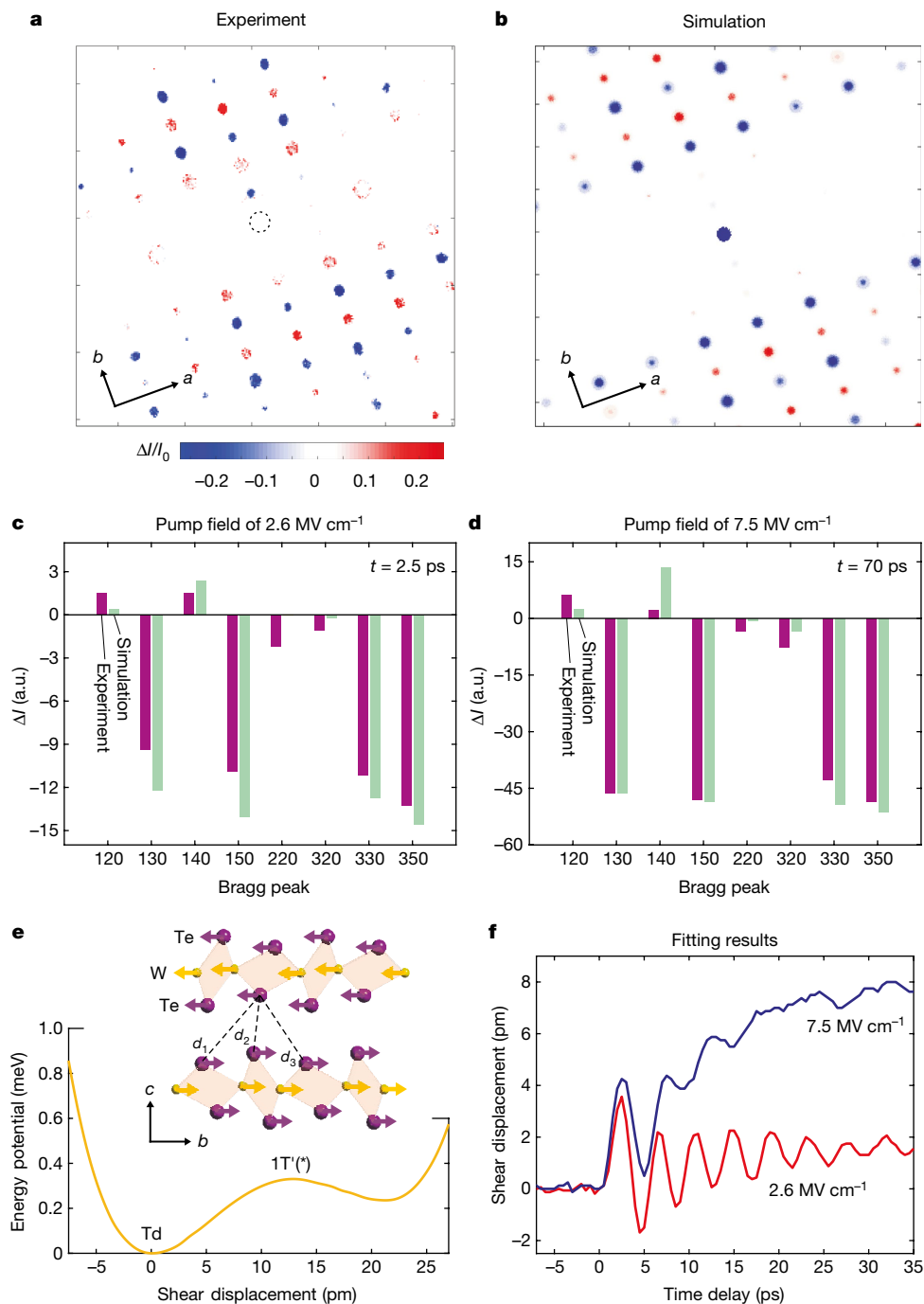


Fig. 2 | Determination of interlayer shear atomic displacements in WTe_2 . **a**, Measured diffraction intensity changes at 2.5 ps, obtained using a pump frequency of 23 THz. The alternating sign changes along the b axis are signatures of shear displacements along the b axis, as shown in the inset of **e**. **b**, Simulated diffraction intensity changes, obtained by rigidly displacing the adjacent WTe_2 layers relative to each other (shear) along the b axis. **c**, **d**, Bar charts showing the ΔI fitting results between the experiment and simulation to obtain Δy at a pump field of 2.6 MV cm^{-1} ($\Delta t = 2.5 \text{ ps}$; **c**) and 7.5 MV cm^{-1} ($\Delta t = 70 \text{ ps}$; **d**); a.u., arbitrary units.

observed photoinduced structural transitions in atomically thin indium wires²⁴. To further understand this, we carried out comparative measurements in a related material, MoTe_2 , which can crystallize in the Td and $1T'$ phases at different temperatures^{25,26}. Whereas in the Td phase we observe light-induced shear displacements, in the $1T'$ phase we observe negligible signals (Methods). This is consistent with a mechanism in which the terahertz fields drive the material unidirectionally towards $1T'$.

e, Energy potential as a function of interlayer shear displacement (see DFT analysis, Methods). The schematic shows an interlayer shear motion along the positive displacement, that is, towards $d_1 < d_3$. The Td phase is the ground-state non-centrosymmetric structure, whereas the $1T'$ phase is an excited-state centrosymmetric structure that is accessible via an interlayer shear displacement. **f**, Shear displacements as a function of time delay at pump fields of 2.6 MV cm^{-1} (red) and 7.5 MV cm^{-1} (blue), obtained through global fitting of the intensity changes of many Bragg peaks.

The ability to drive a shear displacement using terahertz pulses offers a way to manipulate the topological properties of the semimetal WTe_2 on ultrafast timescales. There are a total of eight WPs in the equilibrium Td phase of WTe_2 in the $k_z = 0$ plane. It is sufficient to consider two of these WPs in the $k_x, k_y > 0$ quadrant because we can obtain the remaining six WPs through the time-reversal and mirror symmetries. The two WPs carry opposite chiralities associated with the topological charges $\chi^- = -1$ (WP1) and $\chi^+ = +1$ (WP2), which are connected by a Fermi

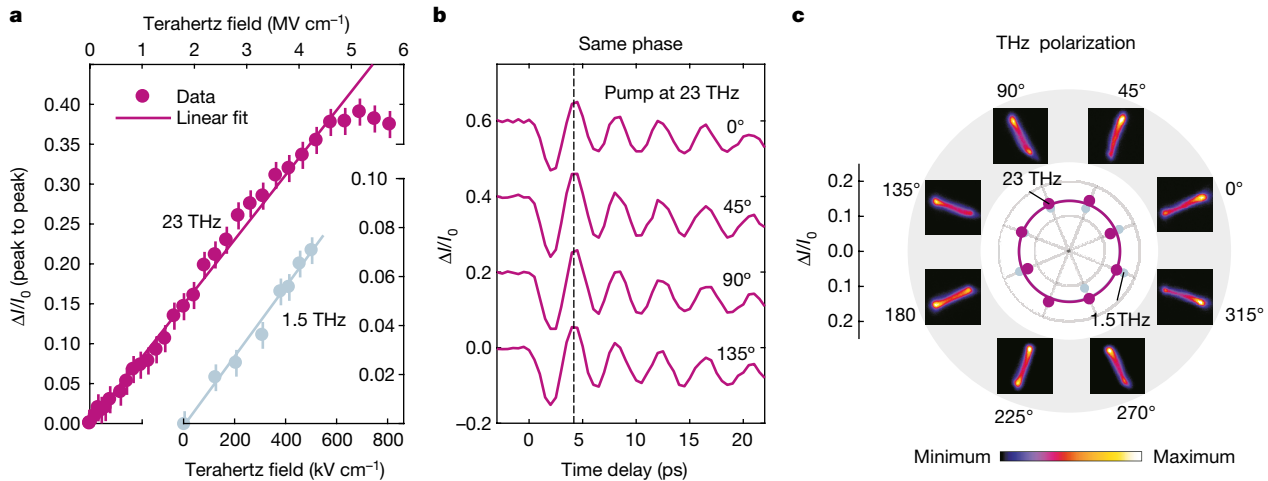


Fig. 3 | Field and polarization dependence of terahertz-induced shear amplitudes. **a**, Bragg peak (130) intensity changes at increasing terahertz-field strength at frequencies of 1.5 THz and 23 THz. Both experiments show a linear dependence with terahertz electric field. The vertical error bars represent standard deviations. **b**, Time trace at various terahertz polarizations (23-THz pump), showing that the modulation always starts at the same phase and amplitude, regardless of the pump polarization. A similar feature is also observed using a 1.5-THz pump. Curves in **b**

arc on the surface. Because the two WPs are separated mainly along k_y , we can expect large changes in the WP separation in momentum space by tuning the hopping parameters and band dispersion through interlayer shear strain along the y axis. In this way, the induced shear strain acts on the Weyl fermions as a chiral gauge-field vector potential, \mathbf{A} , because it couples to WP1 and WP2 with opposite signs in momentum space, $\mathbf{p} \rightarrow (\mathbf{p} - \chi^\pm e\mathbf{A})$, where e is the electron charge.

To demonstrate this, we compute the electronic band structure of WTe_2 using first-principles DFT calculations and monitor the positions of the WPs at different interlayer displacements Δy (Fig. 4a), as determined by our UED results. Our DFT calculations are performed using a Born–Oppenheimer approximation, in which electrons can instantaneously adjust to the new lattice environment. This is particularly appropriate for the interlayer shear mode because its timescale is much longer than that of the electrons, and the use of a terahertz pump does not create substantial electronic excitation. Type II WPs result from crossings between electron and hole bands. Hence, by mapping the energy difference between the two bands in momentum space, the positions of the WPs can be identified as the zero-energy gap position (WP1, blue; WP2, red). At equilibrium ($\Delta y = 0$), the WPs are separated by 0.7% of the reciprocal lattice vector $|\mathbf{G}_2|$. At positive shear displacements, the WPs move towards each other and mutual annihilation occurs at $\Delta y = +2.2$ pm. At negative shear displacements, the WPs move away from each other, leading to a more robust topological structure with more than twofold-increased WP separation. This is consistent with the intuitive picture in which positive shear moves towards a centrosymmetric and trivial phase, whereas negative shear moves towards a non-centrosymmetric and topological phase. At increasingly negative Δy , WP2 approaches the mirror plane at $k_y = 0$ and eventually annihilates with its mirror image of opposite chirality. This leads to a Lifshitz transition from a topological semimetal with eight WPs to one with four WPs, achieving the minimum non-zero number of WPs allowed in a time-reversal invariant system (Fig. 4b).

Although it is challenging to measure the distinct topological phases across the Lifshitz transition, we can experimentally verify the transition from a topological phase to a trivial phase using a time-resolved second-harmonic generation (SHG) technique. In a situation where inversion symmetry in WTe_2 is restored, the electronic phase transition from a topological to a trivial semimetal must follow. This is because the emergence of WP pairs in materials is contingent on lifting the double degeneracy of a Dirac cone by either breaking time-reversal or

are offset for clarity. **c**, Polar plot of the oscillation amplitude at various pump polarizations using frequencies of 1.5 THz (grey circles) and 23 THz (purple circles). The shaded areas show the EMCCD images of the electron-beam transverse displacement by the terahertz field (streaking), as a measure of the terahertz-pump polarization. These results show that the driving mechanism of the shear mode is linear in the applied field strength and isotropic in the polarization.

inversion symmetry. SHG arises from a non-zero second-order susceptibility, as shown in non-centrosymmetric topological systems^{27,28}. Thus, it can be used as a sensitive probe to monitor the inversion symmetry and topological changes in WTe_2 . In this measurement, we use a 2.1- μm -wavelength pump pulse to induce the transition, which gives interlayer shear displacements similar to those induced by terahertz pulses. Figure 4d shows the SHG polarization scans of WTe_2 in the absence of pump pulse (blue), which shows two lobes oriented horizontally. After the pump pulse arrives ($\Delta t = 2$ ps), the SHG vanishes almost completely in all polarizations, with magnitudes comparable to the detection noise level and to the measured SHG signal from centrosymmetric $1\text{T}'\text{MoTe}_2$. Figure 4e shows the measured SHG time trace from WTe_2 at various pump field strengths. At low fields (blue and red curves), the SHG intensity oscillates with the frequency of the shear mode at 0.24 THz. Of particular importance is that the oscillation always starts with a reduced SHG towards a centrosymmetric structure, consistent with our UED results (Fig. 2e, f). At high field (yellow) the SHG intensity plummets drastically, approaching a 100% reduction, which persists beyond the nanosecond timescale (Extended Data Fig. 7c). This indicates that WTe_2 exhibits a phase transition from a non-centrosymmetric to a centrosymmetric phase, consistent with our diffraction studies, and must correspond to a topological-to-trivial phase transition.

Similar manipulations of the WPs in WTe_2 can in principle be obtained through a compressive uniaxial strain along the a axis¹⁶. For example, at 1% uniaxial strain the WP separation is 2.2% of $|\mathbf{G}_2|$, and annihilation of WP2 at the mirror plane occurs at 2% uniaxial strain with energy cost of 32–39 meV per unit cell. This is about 1–2 orders of magnitude larger than the energy required for a shear strain to cause the same effect (Methods), indicating that the interlayer strain provides a more energy-efficient means of manipulating the topological band structure. In addition, shear displacement allows manipulation of WPs at terahertz frequencies. This ultrafast motion of the WPs is associated with a time-varying elastic gauge potential $A(t)$ and yields a pseudoelectric field $E = -\partial A/\partial t$, which can be used as a means of modulating charge density between bulk and surface⁹ and to explore effective gauge fields driven by space- and time-dependent strains^{8,9,29,30}.

These findings offer a new promising way to enhance control over the topological properties of matter by modulating the topological invariants through field-driven lattice deformations. This leads to a substantial motion of the WPs and an ultrafast switch to structures with

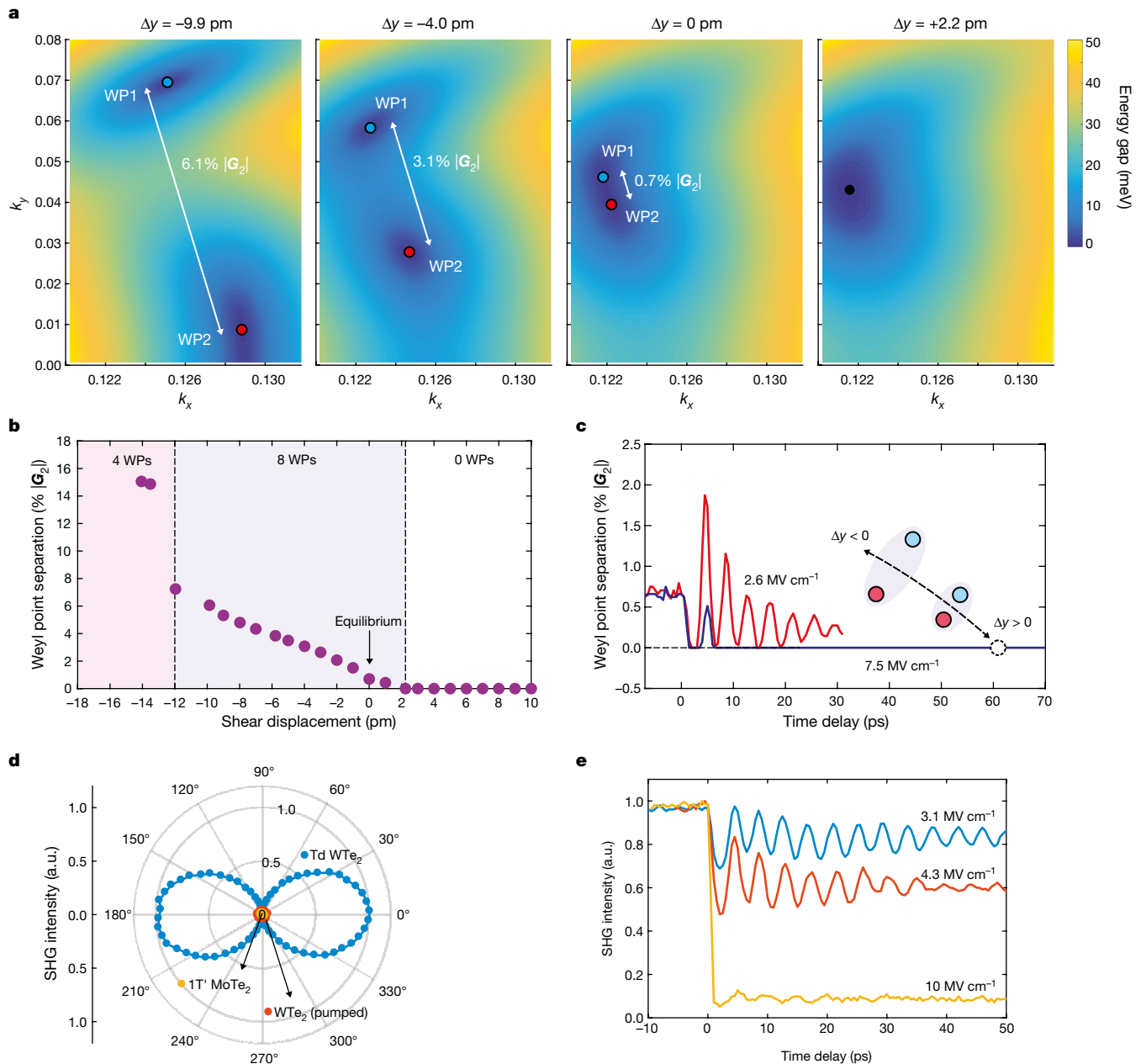


Fig. 4 | Strain-induced WP separation and topological phase transition.

a, The two nearest WPs in momentum space (WP1, blue; WP2, red) at various shear displacements Δy . **b**, Topological phase diagram showing the WP separation as a function of shear displacement, where the number of WPs changes between zero (0 WPs), four (4 WPs) and eight (8 WPs). **c**, Time trace of WP separation upon launching the shear motion using 23-THz pump pulses at fields of 2.5 MV cm^{-1} (red) and 7.5 MV cm^{-1} (blue). At low fluence, the time trace shows a clear oscillation, increasing and decreasing the WP separation. At high fluence, the WPs mostly annihilate

each other. **d**, SHG intensity polar plot of equilibrium WTe_2 (blue), pumped WTe_2 (red) and centrosymmetric MoTe_2 (yellow) at various SHG-polarizer angles, where the transmission axis is aligned horizontally at 0° or vertically at 90° . **e**, Pump-induced SHG time traces of WTe_2 at various pump field strengths. Here, the pump pulse has a wavelength of 2.1 μm (polarized at 45° off the horizontal axis), the incident probe pulse has a wavelength of 800 nm and is vertically polarized, and the crystallographic a axis is aligned horizontally. The SHG results show that WTe_2 exhibits a transition towards a centrosymmetric, topologically trivial phase.

topologically distinct phases, which are potentially useful for applications. In addition, it can be used to stabilize emergent topological phases at non-equilibrium in otherwise trivial materials, thus diversifying the class of topological materials.

Online content

Any methods, additional references, Nature Research reporting summaries, source data, statements of data availability and associated accession codes are available at <https://doi.org/10.1038/s41586-018-0809-4>.

Received: 20 April 2018; Accepted: 25 October 2018;
Published online 2 January 2019.

- Hasan, M. Z. & Kane, C. L. Colloquium: topological insulators. *Rev. Mod. Phys.* **82**, 3045–3067 (2010).
- Burkov, A. A. Topological semimetals. *Nat. Mater.* **15**, 1145–1148 (2016).
- Jia, S., Xu, S. Y. & Hasan, M. Z. Weyl semimetals, Fermi arcs and chiral anomalies. *Nat. Mater.* **15**, 1140–1144 (2016).
- Roushan, P. et al. Topological surface states protected from backscattering by chiral spin texture. *Nature* **460**, 1106–1109 (2009).
- Alpichshev, Z. et al. STM imaging of electronic waves on the surface of Bi_2Te_3 : topologically protected surface states and hexagonal warping effects. *Phys. Rev. Lett.* **104**, 016401 (2010).
- Qian, X. et al. Quantum spin Hall effect in two-dimensional transition metal dichalcogenides. *Science* **346**, 1344–1347 (2014).
- Cortijo, A. et al. Elastic gauge fields in Weyl semimetals. *Phys. Rev. Lett.* **115**, 177202 (2015).

8. Grushin, A. G. et al. Inhomogeneous Weyl and Dirac semimetals: transport in axial magnetic fields and Fermi arc surface states from pseudo-Landau levels. *Phys. Rev. X* **6**, 041046 (2016).
9. Pikulin, D. I., Chen, A. & Franz, M. Chiral anomaly from strain-induced gauge fields in Dirac and Weyl semimetals. *Phys. Rev. X* **6**, 041021 (2016).
10. Zeljkovic, I. et al. Strain engineering Dirac surface states in heteroepitaxial topological crystalline insulator thin films. *Nat. Nanotechnol.* **10**, 849–853 (2015).
11. Liu, Y. et al. Tuning Dirac states by strain in the topological insulator Bi_2Se_3 . *Nat. Phys.* **10**, 294–299 (2014).
12. Xu, S. Y. et al. Discovery of a Weyl fermion semimetal and topological Fermi arcs. *Science* **349**, 613–617 (2015).
13. Yang, L. X. et al. Weyl semimetal phase in the non-centrosymmetric compound TaAs. *Nat. Phys.* **11**, 728–732 (2015); erratum **11**, 879 (2015).
14. Lv, B. Q. et al. Experimental discovery of Weyl semimetal TaAs. *Phys. Rev. X* **5**, 031013 (2015).
15. Ali, M. N. et al. Large, non-saturating magnetoresistance in WTe_2 . *Nature* **514**, 205–208 (2014).
16. Soluyanov, A. A. et al. Type-II Weyl semimetals. *Nature* **527**, 495–498 (2015).
17. Li, P. et al. Evidence for topological type-II Weyl semimetal WTe_2 . *Nat. Commun.* **8**, 2150 (2017).
18. Lin, C. L. et al. Visualizing type-II Weyl points in tungsten ditelluride by quasiparticle interference. *ACS Nano* **11**, 11459–11465 (2017).
19. Lv, Y. Y. et al. Experimental observation of anisotropic Adler–Bell–Jackiw anomaly in type-II Weyl semimetal $\text{WTe}_{1.98}$ crystals at the quasiclassical regime. *Phys. Rev. Lett.* **118**, 096603 (2017).
20. Yang, J. et al. Elastic and electronic tuning of magnetoresistance in MoTe_2 . *Sci. Adv.* **3**, eaao4949 (2017).
21. Weathersby, S. P. et al. Mega-electron-volt ultrafast electron diffraction at SLAC National Accelerator Laboratory. *Rev. Sci. Instrum.* **86**, 073702 (2015).
22. Kim, H.-J. et al. Origins of the structural phase transitions in MoTe_2 and WTe_2 . *Phys. Rev. B* **95**, 180101 (2017).
23. Nicoul, M. et al. Picosecond acoustic response of a laser-heated gold-film studied with time-resolved X-ray diffraction. *Appl. Phys. Lett.* **98**, 191902 (2011).
24. Frigge, T. et al. Optically excited structural transition in atomic wires on surfaces at the quantum limit. *Nature* **544**, 207–211 (2017).
25. Chen, S. Y. et al. Activation of new Raman modes by inversion symmetry breaking in type II Weyl semimetal candidate T' - MoTe_2 . *Nano Lett.* **16**, 5852–5860 (2016).
26. Zhang, K. et al. Raman signatures of inversion symmetry breaking and structural phase transition in type-II Weyl semimetal MoTe_2 . *Nat. Commun.* **7**, 13552 (2016).
27. Morimoto, T. & Nagaosa, N. Topological nature of nonlinear optical effects in solids. *Sci. Adv.* **2**, e1501524 (2016).
28. Wu, L. et al. Giant anisotropic nonlinear optical response in transition metal mononitride Weyl semimetals. *Nat. Phys.* **13**, 350–355 (2017).
29. Levy, N. et al. Strain-induced pseudo-magnetic fields greater than 300 tesla in graphene nanobubbles. *Science* **329**, 544–547 (2010).
30. Gomes, K. K. et al. Designer Dirac fermions and topological phases in molecular graphene. *Nature* **483**, 306–310 (2012).

Acknowledgements This work is supported primarily by the US Department of Energy (DOE), Office of Basic Energy Sciences, Division of Materials Sciences and Engineering, under contract number DE-AC02-76SF00515, the Stanford Linear Accelerator (SLAC) National Accelerator Laboratory, the Stanford Institute for Materials and Energy Sciences (E.J.S., C.M.N., C.D.P., E.M., T.P.D.,

T.F.H., A.M.L.). E.J.S. acknowledges additional support from Stanford GLAM Postdoctoral Fellowship Program. C.M.N. acknowledges additional support from the National Science Foundation (NSF) through a Graduate Research Fellowship (DGE-114747). T.F.H. acknowledges additional funding for analysis from the Gordon and Betty Moore Foundation EPIQS Initiative through grant number GBMF4545. S.J.P. is supported by the US Department of Energy (DE-SC0012375). M.C.H. is supported by the US Department of Energy, Office of Science, Office of Basic Energy Sciences, under award number 2015-SLAC-100238-Funding. B.K.O.-O. acknowledges support from the DOE Office of Science, Fusion Energy Science, under grant number FWP 100182. N.F. acknowledges support from the Stewardship Science Graduate Fellowship programme, provided under cooperative agreement number DE-NA0002135. Synthesis of MoTe_2 and sample preparation were supported by the US Department of Energy, DE-SC0016703 (D.R., D.C., A.A., J.H.). L.B. acknowledges the US Army Research Office MURI grant W911NF-11-1-0362. The National High Magnetic Field Laboratory is supported by the NSF through NSF/DMR-1157490, NSF/DMR-1644779 and the State of Florida. First-principles calculations by C.D.P. were supported by the TIMES programme at SLAC. Numerical simulations were performed using computational resources at the National Energy Research Scientific Computing Center (NSERC). The UED work was performed at SLAC MeV-UED, which is supported in part by the DOE BES SUF Division Accelerator & Detector R&D programme, the LCLS Facility and SLAC under contracts DE-AC02-05-CH11231 and DE-AC02-76SF00515. The authors thank D. Pikulin and B. Moritz for discussions and G. Stewart for the illustration of the UED setup.

Reviewer information *Nature* thanks C. Ropers and the other anonymous reviewer(s) for their contribution to the peer review of this work.

Author contributions E.J.S., C.M.N. and A.M.L. conceived the experiments, analysed and interpreted the data; E.J.S. and C.M.N. performed the SHG experiments, analysed and interpreted the data with A.M.L. and T.F.H.; E.J.S., C.M.N., A.M.L. and C.D.P. wrote the manuscript with input from all authors; E.J.S. and C.M.N. performed the UED experiments with S.J.P., X.S., J.Y., R.L., S.W., E.M. and X.J.W.; B.K.O.-O., M.C.H. and A.H.R. implemented the terahertz setup; D.R., L.B., C.M.N., E.J.S., N.F., D.C., A.A., J.H. and T.F.H. synthesized the crystals and prepared the samples; C.D.P. and T.P.D. performed the first-principles calculations; X.J.W. led the SLAC 3-MeV UED and terahertz-pump UED-probe development. All authors discussed the results and contributed to the writing of the manuscript.

Competing interests E.J.S., C.M.N., C.D.P., X.J.W. and A.M.L. have submitted a patent application (“Fast topological switch using strained Weyl semimetals”; US number 62/726,893) that covers a specific aspect of the manuscript. The other authors declare no competing interests.

Additional information

Extended data is available for this paper at <https://doi.org/10.1038/s41586-018-0809-4>.

Supplementary information is available for this paper at <https://doi.org/10.1038/s41586-018-0809-4>.

Reprints and permissions information is available at <http://www.nature.com/reprints>.

Correspondence and requests for materials should be addressed to A.M.L.

Publisher’s note: Springer Nature remains neutral with regard to jurisdictional claims in published maps and institutional affiliations.

METHODS

Sample synthesis and preparation. High-quality single crystals of WTe_2 were synthesized using a self-flux method in excess of Te. W 99.999% and Te 99.9999% powders were placed in a quartz ampoule in a ratio of 1:25, heated to 1,100 °C and held at this temperature for three days. Subsequently, the ampoule was slowly cooled to 525 °C over two weeks and centrifuged. The ‘as-harvested’ single crystals were then annealed for two days at a temperature of 425 °C under a temperature gradient to remove excess Te. To prepare the synthesized samples for UED experiments, WTe_2 was mechanically exfoliated onto a SiO_2/Si substrate using a standard mechanical exfoliation technique. From the exfoliated crystal, the samples were selected for subsequent transfer by their size ($>50 \mu\text{m}$ in the lateral dimension) and thickness ($>50 \text{nm}$). After verifying the thickness using an atomic force microscope, poly(propylene carbonate) (PPC) in anisole solution (15% PPC by weight) was spun onto the WTe_2 -covered SiO_2/Si substrate at a rate of 1,500 r.p.m. with an acceleration of 1,000 r.p.m. s^{-1} for 1 min and then heated to 80 °C for 2 min on a hotplate. The PPC film and the WTe_2 crystal were then peeled from the substrate and suspended over a hotplate with the WTe_2 facing up. A 50-nm-thick Si_3N_4 transmission-electron-microscopy membrane was then aligned over the suspended crystal using an optical microscope, and placed on the PPC film while raising the temperature to 115 °C to induce contact between the WTe_2 crystal and the membrane. The sample was then soaked in acetone for 10 min to remove the PPC, gently rinsed with isopropyl alcohol and dried under a flow of nitrogen gas, thus completing the transfer.

SLAC 3-MeV UED setup. We used a relativistic UED technique to reconstruct the shear motion and crystallographically measure the corresponding atomic displacements through the measurement of more than 200 Bragg peaks (Fig. 1b). The electron beam is generated using a frequency-tripled Ti:sapphire laser by excitation of a copper photocathode and rapidly accelerated to 3 MeV in radiofrequency electric fields²¹. The pulse duration of the electron beam at the sample position is 150 fs. Magnetic lenses are used to steer and focus the electron beam³¹ onto the sample, an exfoliated single-domain crystal, with a spot size of 100 μm . The diffracted electron beam is captured in a transmission geometry using an electron-multiplying CCD camera. We used two different pump excitation schemes in this experiment: a quasi-single-cycle excitation at 1–5 THz and a few-cycle excitation at 23 THz. The arrival time of the electron beam (probe) could be adjusted with respect to the terahertz pulses (pump) using an optical delay stage.

Ultrafast terahertz sources. Quasi-single-cycle terahertz pulses were generated by optical rectification of 1,350-nm near-infrared laser pulses in the organic nonlinear crystals DSTMS (4-N,N-dimethylamino-4'-N'-methyl-stilbazolium 2,4,6-trimethylbenzenesulfonate)³² and OH-1 (2-(3-(4-hydroxystyryl)-5,5-dimethylcyclohex-2-enylidene)malononitrile)³³. The 1,350-nm near-infrared pulses were generated from an 800-nm Ti:sapphire laser system in a three-stage optical parametric amplifier system (Light Conversion HE-TOPAS) and had pulse energies up to 2 mJ and a pulse duration of about 50 fs.

The terahertz field was brought to an intermediate focus with an off-axis parabolic mirror with 2-inch (50.8 mm) focal length, collimated with a second mirror with 6-inch (152.4 mm) focal length. The collimated beam was transported into the UED diffraction chamber via a polymer window and focused with an off-axis parabolic mirror with 3-inch (76.2 mm) focal length inside the chamber. The terahertz field was characterized at the sample location by electro-optical sampling using a split-off portion of the 800-nm laser and a 50- μm -thick 110-cut GaP crystal. The observed peak field strength of the DSTMS-generated terahertz pulse was 650 kV cm^{-1} , with the spectrum centred at about 3 THz when using an 8-mm-diameter 450- μm -thick crystal and input pump pulse energy of about 1 mJ. With a 10-mm-diameter clear aperture and a 500- μm -thick OH-1 crystal, the peak field strength was 500 kV cm^{-1} , with the spectrum peaked at 1.5 THz and sizeable spectral components extending to about 3.5 THz (Extended Data Fig. 2). The polarization of the terahertz pulses was linear and the polarization angle could be changed arbitrarily by rotating the generation crystal together with the pump-pulse polarization. A detailed discussion of the experimental apparatus can be found in ref. ³⁴.

Mid-infrared (MIR) pulses with 13- μm wavelength (23 THz frequency) were generated by difference-frequency generation in GaSe from the signal and idler of the same optical parametric amplifier system (Light Conversion HE-TOPAS), driven by 800-nm pulses with duration of about 130 fs. Here the signal and idler wavelengths were 1,505 nm and 1,705 nm, respectively. The MIR beam was transported into the experimental chamber through a 3-mm-thick KRS-5 window and focused with an off-axis parabolic mirror with 3-inch (76.2 mm) focal-length. A pair of holographic wire-grid polarizers (Thorlabs WP25H-K) was used to attenuate the pulse energy to the desired level. The pulse duration of the MIR pulses was of the order of 300 fs after taking into account dispersion. MIR spot-size measurements at the sample position were obtained with a DataRay WinCamD beam profiler.

Structure factor calculation with interlayer shear displacement. The intensity of a Bragg peak, $I \propto |S|^2$, can be calculated using the general form of the structure factor

$$S(hkl) = \sum_j f_j \exp[-i2\pi(hx_j + ky_j + lz_j)] \quad (2)$$

where the summation runs over all atoms in the unit cell (four W and eight Te atoms), f_j is the atomic scattering factor for the j th atom, $\mathbf{r}_j = x_j\hat{a} + y_j\hat{b} + z_j\hat{c}$ is the vector position of the atom in the unit cell ($0 \leq x, y, z \leq 1$) and (hkl) are the usual Miller indices. Because we use transmission geometry at the $[001]$ zone axis, the diffraction image shows only the $l = 0$ peaks, that is, $(hk0)$. We calculate the peak intensity modulation $\Delta I/I_0$ by introducing the top-layer shear displacement Δy with respect to the bottom layer into the structure factor

$$S(\Delta y) = \exp(-i2\pi k\Delta y) \sum_{\text{top}} f_j \exp[-i2\pi(hx_j + ky_j)] + \sum_{\text{bottom}} f_j \exp[-i2\pi(hx_j + ky_j)] \quad (3)$$

We can obtain a more symmetric expression by having the shear displacement shared equally between the two layers ($\Delta y/2$), that is, by multiplying with a common phase factor $\exp(+i\pi k\Delta y)$ and by using the underlying crystal symmetry through (i) a reflection with respect to the b - c mirror plane ($x \rightarrow -x$) and (ii) a non-symmorphic C_2 transformation. The latter consists of a reflection with respect to the a - c mirror plane ($y \rightarrow -y$) and a translation along the a - c axis $(+0.5, 0, +0.5)$. These symmetry operations project each atom from the bottom layer to the top layer

$$S(\Delta y) = \exp(-i\pi k\Delta y) \sum_{\text{top}} f_j \exp[-i2\pi(hx_j + ky_j)] + \exp(+i\pi k\Delta y) \sum_{\text{top}} f_j \exp[+i2\pi(hx_j + ky_j)] \quad (4) = 2 \sum_{\text{top}} f_j \cos[2\pi(hx_j + ky_j) + \pi k\Delta y]$$

Now the summation runs over all atoms in the top half of the unit cell (two W and four Te atoms). To compare this with our experiment, we calculated the change of peak intensity $\Delta|S(\Delta y)|^2 = |S(\Delta y)|^2 - |S(0)|^2$ using known x_j and y_j values¹⁶, as shown in Fig. 2b. The structure factors f_j were calculated using X-ray-scattering factors from published analytical fits^{35,36} converted to electron-scattering factors using the Mott-Bethe formula³⁷. Here, we define a positive shear displacement ($\Delta y > 0$) as shown in the inset of Fig. 2e.

Fitting of the structural-factor modulations. For each time point Δt , the mean-square error (P) is calculated for a range of shear displacements Δy for a selection of m Bragg peaks (hkl) . In addition, an anisotropic (elliptical) Debye-Waller factor is included to account for heating effects in the sample, which is considerably smaller than those from the shear displacements due to the low pump photon energy (terahertz). The mean squared error is

$$P(\Delta y, \langle u_a^2 \rangle, \langle u_b^2 \rangle) = \frac{1}{m} \sum_{hkl} \left[\frac{\Delta I}{I_0}(hkl, \Delta y, \langle u_a^2 \rangle, \langle u_b^2 \rangle)_{\text{sim}} - \frac{\Delta I}{I_0}(hkl)_{\text{exp}} \right]^2$$

where $\langle u_a^2 \rangle$ and $\langle u_b^2 \rangle$ are the mean-square atomic displacements along the a and b axes, respectively, which affect the intensity of a Bragg peak by the Debye-Waller relation, $I = I_0 \exp[-\frac{1}{2}(Q_a^2 \langle u_a^2 \rangle + Q_b^2 \langle u_b^2 \rangle)]$, with a time constant determined by the (400) Bragg peak. Here, Q_a and Q_b are the projections of \mathbf{Q} , the reciprocal lattice vector of the Bragg peak, along the a and b axes. The simulated intensity change, $(\Delta I/I_0)_{\text{sim}}$, has the form

$$\frac{\Delta I}{I_0}(hkl, \Delta y, \langle u_a^2 \rangle, \langle u_b^2 \rangle)_{\text{sim}} = \frac{|S(\Delta y)|^2 e^{-\frac{1}{2}(Q_a^2 \langle u_a^2 \rangle + Q_b^2 \langle u_b^2 \rangle)} - |S(0)|^2}{|S(0)|^2}$$

Here, $S(\Delta y)$ is the structure factor calculated for a given Δy , as discussed in the main text, and $S(0)$ is the structure factor calculated for the undistorted structure. The values for each parameter Δy , $\langle u_a^2 \rangle$ and $\langle u_b^2 \rangle$ at every Δt are optimized by minimizing P . In other words, the fitting procedure is performed to minimize the peak intensity difference between experiment and simulation and is averaged across many Bragg peaks.

Estimating the effective terahertz-induced hole doping. We use a simple Drude model to estimate the effective hole doping. The fraction of electrons that contribute to the resulting current is v/v_F , where v is the drift velocity and v_F is the Fermi velocity. The drift velocity can be estimated through $v = eE\tau/m$, where e is the electron charge, E is the applied electric field, τ is the scattering time and m is the effective mass. By using the reported values¹⁷ of $m \approx 0.4m_e$ (m_e , electron mass),

$v_F \approx 3 \times 10^5 \text{ m s}^{-1}$, a typical value of $\tau \approx 10 \text{ fs}$ in a semimetal and $E \approx 1 \text{ MV cm}^{-1}$, we found that $v \approx v_F$. For a hole pocket with carrier density of $n_0 \approx 7 \times 10^{19} \text{ cm}^{-3}$ in WTe_2 ³⁸, this is comparable with an effective hole doping density required for the Td–1T' phase transition²² as the impulsive driving force for the interlayer shear motion. Moreover, recent experiments reported considerably larger scattering time values of $\tau > 100 \text{ fs}$ in WTe_2 ^{17,39}. This suggests that an even larger electron density can be transiently transferred away from the topmost valence band by the terahertz pump field to induce the interlayer shear motion. We note that the terahertz-induced effective doping serves as an impulsive driving force to kick-start the shear mode and does not require the excited carriers to be maintained during the long-lived metastable phase. Such a metastable phase persists for a time that is determined by the energy barrier of the local potential minimum and thermal fluctuations.

DFT analysis. DFT^{40,41} simulations of WTe_2 were carried out to ascertain the energetics of the experimentally observed 0.24-THz shear mode of interest (Fig. 2e) and the Brillouin-zone (BZ) motion of WPs resulting from atomic displacements associated with this mode. The topological characteristics of the electronic band structure of Td WTe_2 have been explored previously^{16,22}. In particular, Soluyanov et al.¹⁶ investigated the type II Weyl semimetal character of Td WTe_2 partly on the basis of DFT band-structure simulations carried out at the experimentally observed geometry⁴². More recently, Kim et al.²² studied the effect of geometry optimization, within the van der Waals (vdW) DFT framework⁴³, on the WPs in Td WTe_2 . They found that the stability of Weyl nodes in WTe_2 is sensitive to lattice parameter differences of the order of 1%; in fact, owing to slight (about 1%) inaccuracies in the vdW–DFT-predicted a and c parameters, WPs of opposite chiralities annihilate at the vdW–DFT equilibrium geometry of WTe_2 , rendering it a trivial semimetal. To recover distinct Weyl nodes in the BZ, small strains need to be applied²².

To circumvent the issues related to the sensitive dependence on specific vdW–DFT geometries, we initially employ as reference the experimental geometry⁴² used in the work of Soluyanov et al.¹⁶ to carry out our analysis of the BZ motion of the Weyl nodes in WTe_2 under the influence of shear-mode displacements along the y axis (crystallographic b axis). This geometry is characterized by an orthorhombic (Td) lattice with parameters $a = 3.477 \text{ \AA}$, $b = 6.249 \text{ \AA}$ and $c = 14.018 \text{ \AA}$. W and Te atoms occur at the 2a Wyckoff positions parameterized as $(0, y, z)$ and $(1/2, -y, z+1/2)$ for values of y, z given in Extended Data Table 1a (reproduced from Soluyanov et al.¹⁶). Simulations in this context are carried out using the DFT framework as implemented in the Vienna ab initio simulation package⁴⁴ (VASP) version 5.4.1. All calculations include spin–orbit coupling within the non-collinear DFT formalism. Exchange–correlation effects are treated at the level of the generalized gradient approximation through the PBE⁴⁵ functional. Projector-augmented-wave⁴⁶ potentials with valence electronic configurations of $\{6s^2, 5d^4\}$ for W and $\{5s^2, 5p^4\}$ for Te are employed in conjunction with a plane-wave energy cutoff parameter of 260 eV. For electron density convergence, a Γ -centred $12 \times 10 \times 6$ k -point grid and Gaussian smearing with a smearing parameter of 0.05 eV are used. The simulation parameters here are similar to those adopted in Soluyanov et al.¹⁶. WP positions in the $k_z = 0$ plane of the BZ of WTe_2 are subsequently identified through band-structure calculations employing a dense $43 \times 85 \times 1$ k -point mesh spanning a sub-region of the $(k_x, k_y, k_z = 0)$ plane, as shown in Fig. 4a. At the employed geometry, we identify two WPs (WP1, WP2) in the first quadrant of the $k_z = 0$ plane of the BZ at the coordinates shown in Extended Data Table 1b. The remaining six points in the other three quadrants are related to these by reflections in the $k_x = 0$ and $k_y = 0$ planes¹⁶. The coordinates identified here are similar to those reported in the literature^{16,22}.

Phonon band-structures are calculated within the frozen-phonon finite-difference approach using the *phonopy*⁴⁷ code interfaced with VASP. In Extended Data Fig. 3a, the phonon band dispersions of Td WTe_2 at the experimental reference geometry are plotted along high-symmetry lines in the $k_z = 0$ plane. At the Γ point, the low-energy mode at 0.29 THz is unambiguously identified as the relevant interlayer shear mode of interest, which corresponds to the 0.24-THz mode observed experimentally. This identification is facilitated by the absence of any other modes at similar energies and also by inspecting the atomic position modulations associated with the mode eigenvector. As denoted in Fig. 2e of the main text, this mode predominantly involves a relative shear displacement along the b axis of adjacent WTe_2 layers in the unit cell. To investigate the motion of WPs in the BZ induced by this mode, first a number of unit-cell geometries modulated along the mode displacement coordinate are generated using the *phonopy* code. Subsequently, the DFT electronic-band structures corresponding to these modulated geometries are calculated, and the positions of WPs in the BZ are mapped as a function of displacement along the mode coordinate, as shown in Fig. 4a. As explained in the main text in connection with Fig. 4a, depending on the sign of the shear-mode displacement along the b axis, pairs of WPs either move closer or farther apart in the BZ, leading to different kinds of topological transitions.

In topological semimetals such as WTe_2 , the positions of WPs in the BZ can be tuned by applying strain. Soluyanov et al.¹⁶ explored changes in the relative positions

of Weyl nodes in WTe_2 induced by uniaxial tensile and compressive strains applied along different crystallographic axes. They report that whereas stretching along the a axis leads to annihilation of all pairs of Weyl nodes, compressive strain along this direction leads to increased separation within each pair of WPs, until half the points eventually annihilate on the $k_y = 0$ mirror plane, leading to a state where only four Weyl nodes survive. As explained in the analysis accompanying Fig. 4, we find that a similar motion of the WPs can be induced via an alternative mechanism, namely, terahertz-pump-induced phonon modulations associated with the 0.24-THz shear mode along the b axis. It is therefore instructive to evaluate the relative energy cost associated with these two approaches to tuning the topological properties of WTe_2 . To this end, we compare DFT total energies of different strained and phonon-modulated structures associated with the WP motion described in Fig. 4. Calculating the total energy cost under different deformations of the lattice requires identifying the minimum energy point associated with the equilibrium geometry. Therefore, for this analysis, we first carry out geometry optimizations within the dispersion corrected DFT-D3⁴⁸ framework including spin–orbit coupling, as implemented in VASP. A plane-wave cutoff of 400 eV, in conjunction with a Γ -centred $16 \times 9 \times 4$ k -point grid, is employed in this instance. As before, exchange–correlation effects are modelled using the PBE functional; additionally, dispersion corrections are incorporated at the level of the DFT-D3⁴⁸ approximation. In particular, for reasons explained below, two different forms for the dispersion corrections are investigated, namely, DFT-D3¹¹ (labelled D3) and DFT-D3 with Becke–Johnson damping⁴⁹ (labelled D3-BJ). The lattice parameters and relevant interlayer distances d_1, d_2, d_3 (see Fig. 2e) in Td WTe_2 predicted by the two methods are listed in Extended Data Table 1c and compared to experimental values.

The last column of Extended Data Table 1c shows the calculated and experimental phonon frequency for the b -axis shear mode. As mentioned earlier, this mode is well approximated as a rigid relative motion along the b axis of the two WTe_2 layers in the unit cell (see Extended Data Fig. 3a). The potential energy associated with this motion is predominantly determined by the interlayer vdW interaction, at least for small displacements, and therefore exhibits a strong dependence on the way that the dispersion corrections are approximated in DFT. We note that whereas the D3 method yields lattice parameters that are within 0.5% of the experimental values, the b -axis shear-mode phonon frequency is underestimated by about 37%. On the other hand, the D3-BJ approximation predicts a mode frequency that is overestimated by about 40%. In the harmonic approximation within which the phonon frequency is estimated, this corresponds to a picture where the potential energy surface associated with displacement along the shear mode is too shallow and too steep in the D3 and D3-BJ approximations, respectively. Although neither method is quantitative, we expect that the correct description lies between the two limits represented by D3 and D3-BJ. With this understanding, we provide here an order-of-magnitude comparison between the relevant strain and phonon modulation energies for driving WP motion in WTe_2 . With reference to the equilibrium geometry, the total energy cost per unit cell as a function of applied compressive strain along the a axis is shown in Extended Data Fig. 3b. Similarly, the total energy cost associated with structural modulation by the b -axis shear phonon as a function of displacement along the mode coordinate is shown in Extended Data Fig. 3c. The displacement (in picometres) along the b axis of one of the W atoms is used as a proxy for the mode coordinate. To annihilate two pairs of Weyl nodes at the $k_y = 0$ mirror plane, either a 2% a -axis compressive strain¹⁶ or a negative displacement of about 12 pm in the sense of Fig. 2e is required. On a per-unit-cell basis, in the D3 (D3-BJ) approximation the former mechanism has an energy cost of 32 meV (39 meV) whereas the latter costs 0.33 meV (3.6 meV). Thus, for driving the topological transition from eight to four Weyl nodes, the lattice strain mechanism is 1–2 orders of magnitude more expensive compared to the phonon-driven mechanism in terms of energy. This is expected because an a -axis strain involves compressing or elongating strong covalent bonds within each layer of WTe_2 , whereas b -axis shear mode involves primarily interlayer interactions, which are weaker.

Longitudinal acoustic-wave timescale. In WTe_2 , the stable Td phase appears as an orthorhombic unit cell in which the b and c axes form an angle of $\theta = 90^\circ$, whereas the 1T' phase appears as a monoclinic unit cell with a 94° angle (Extended Data Fig. 1). Hence, we can expect the Td–1T' transition in WTe_2 to be limited by the time required for the development of an overall shear across the sample thickness (c axis), as determined by the transverse acoustic group velocity. Although we are not aware of any prior measurements on the transverse acoustic velocity, we can take the longitudinal acoustic speed of sound⁵⁰ ($2,000 \text{ m s}^{-1}$) as a first approximation. Hence, we can estimate the build-up time using $t = d/v$, where $d = 50 \text{ nm}$ is the sample thickness and $v = 2,000 \text{ m s}^{-1}$ is the speed of sound, and obtain $t = 25 \text{ ps}$. This is in good agreement with our observation (Fig. 2f, blue line). We can take a separate confirmation of the longitudinal acoustic speed of sound by tilting the sample (pitch of -8.3° , yaw of -13.9°), providing sensitivity to the acoustic breathing mode oscillations (period of $2d/v$) across the sample thickness. The structural-factor modulation $\Delta I/I_0$ of peak (133) shows oscillations with period of 38 ps (Extended Data Fig. 4). Given the period of this oscillation,

we compute the speed of sound to be $v \approx 2,600 \text{ m s}^{-1}$, in reasonable agreement with the above estimate.

Terahertz-induced shear motion in MoTe₂. We discussed in the main text how the shear motion in WTe₂ is driven through a transient hole doping induced by the terahertz field. This interpretation is motivated by a theoretical prediction that upon hole doping the Td phase becomes unstable against the 1T' phase²². A particularly strong indication from our experiment is that at any terahertz-field polarization, the initial shear motion always occurs along the pathway towards a phase transition from the Td phase to the 1T' phase. Hence, this process must be very sensitive to the initial structural phase of the sample, that is, it should only occur in the Td phase and not in the 1T' phase—a feature that can be tested. In particular, we should expect the absence of terahertz-induced shear motion in 1T' MoTe₂. MoTe₂ and WTe₂ have similar structural and electronic properties; unlike WTe₂, however, MoTe₂ can appear in two structural phases: the Td phase below 200 K, the 1T' phase above 250 K and a mixed Td–1T' phase²⁵ at 200–250 K. We performed similar terahertz-pump UED-probe experiments on MoTe₂ at sample temperatures of 28 K (Td) and 300 K (1T') (Extended Data Fig. 5). We found that the interlayer shear oscillations only occur in the Td phase (0.37 THz), and not in the 1T' phase of MoTe₂, where only a small heating (Debye–Waller) effect is observed. This is consistent with the picture that terahertz-induced hole doping stabilizes the 1T' phase over the Td phase. That is, if we start with the Td phase, the relative energy order is reversed upon terahertz-induced hole doping and shear motion is launched; but if we start with the 1T' phase, the relative energy order does not change and no shear motion is observed.

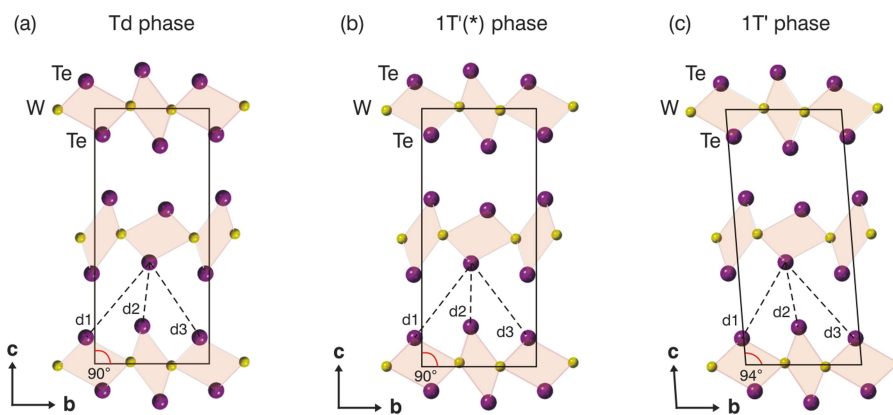
Transition region at intermediate pump fluence. The UED time traces (Fig. 2f) show that the oscillation period is slightly longer at larger pump field strengths. To investigate this transition region, we carried out an additional terahertz-pump UED-probe experiment at smaller pump fluence intervals (Extended Data Fig. 6a, b). As we can see, the oscillation period increases at higher pump fluences. This observation indicates a nonlinear phonon softening towards a new metastable centrosymmetric structure.

Lifetime of excited electrons. The lifetime of excited electrons can be determined from the pump-induced probe reflectivity as a function of time. We carried out an optical pump-probe experiment using 2.1- μm pump and 800-nm probe pulses on a WTe₂ sample (Extended Data Fig. 7a). We note that we replace the role of the terahertz pump with a 2.1- μm pump because the terahertz pump setup that we used for UED requires a special laser specification and is currently not accessible for optical reflectivity experiments. Nevertheless, measurements with 2.1- μm pump pulses can also induce the shear oscillations that we obtained using terahertz pump pulses (Extended Data Fig. 7b). Extended Data Fig. 7a shows an abrupt pump-induced change of probe reflectivity within the first 5 ps and a stable finite reflectivity afterwards for a timescale longer than 50 ps. The first 5 ps can be attributed to relaxation of hot carriers towards a new quasi-equilibrium state. Afterwards, the carriers remain in the new equilibrium state for longer than 50 ps.

Data availability

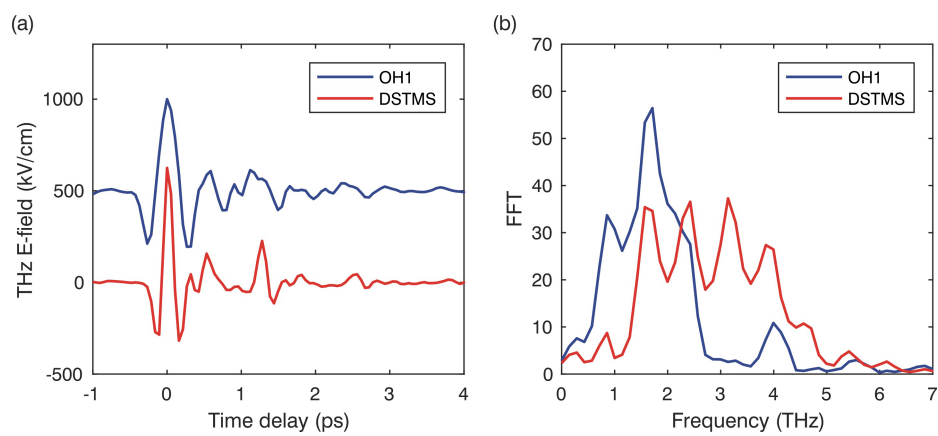
The data that support the findings of this study are available from the corresponding author on reasonable request.

- Shen, X. et al. Femtosecond mega-electron-volt electron microdiffraction. *Ultramicroscopy* **184**, 172–176 (2018).
- Yang, Z. et al. Large-size bulk and thin-film stilbazolium-salt single crystals for nonlinear optics and THz generation. *Adv. Funct. Mater.* **17**, 2018–2023 (2007).
- Brunner, F. D. et al. A hydrogen-bonded organic nonlinear optical crystal for high-efficiency terahertz generation and detection. *Opt. Express* **16**, 16496–16508 (2008).
- Ofori-Okai, B. K. et al. A terahertz pump mega-electron-volt ultrafast electron diffraction probe apparatus at the SLAC Accelerator Structure Test Area facility. *J. Instrum.* **13**, P06014 (2018).
- Waasmaier, D. & Kirfel, A. New analytical scattering-factor functions for free atoms and ions. *Acta Crystallogr. A* **51**, 416–431 (1995).
- Su, Z. & Coppens, P. Relativistic X-ray elastic scattering factors for neutral atoms $Z = 1–54$ from multiconfiguration Dirac–Fock wavefunctions in the $0–12 \text{ \AA}^{-1} \sin\theta/\lambda$ range, and six-Gaussian analytical expressions in the $0–6 \text{ \AA}^{-1}$ range. *Acta Crystallogr. A* **53**, 749–762 (1997).
- De Graef, M. *Introduction to Conventional Transmission Electron Microscopy* (Cambridge Univ. Press, Cambridge, 2003).
- Zhu, Z. et al. Quantum oscillations, thermoelectric coefficients, and the Fermi surface of semimetallic WTe₂. *Phys. Rev. Lett.* **114**, 176601 (2015).
- Homes, C. C., Ali, M. N. & Cava, R. J. Optical properties of the perfectly compensated semimetal WTe₂. *Phys. Rev. B* **92**, 161109 (2015).
- Hohenberg, P. & Kohn, W. Inhomogeneous electron gas. *Phys. Rev.* **136**, B864–B871 (1964).
- Kohn, W. & Sham, L. J. Self-consistent equations including exchange and correlation effects. *Phys. Rev.* **140**, A1133–A1138 (1965).
- Mar, A., Jobic, S. & Ibers, J. A. Metal-metal vs tellurium-tellurium bonding in WTe₂ and its ternary variants TaIrTe₄ and NbIrTe₄. *J. Am. Chem. Soc.* **114**, 8963–8971 (1992).
- Hamada, I. van der Waals density functional made accurate. *Phys. Rev. B* **89**, 121103 (2014).
- Kresse, G. & Furthmüller, J. Efficient iterative schemes for ab initio total-energy calculations using a plane-wave basis set. *Phys. Rev. B* **54**, 11169–11186 (1996).
- Perdew, J. P., Burke, K. & Ernzerhof, M. Generalized gradient approximation made simple. *Phys. Rev. Lett.* **77**, 3865–3868 (1996).
- Blöchl, P. E. Projector augmented-wave method. *Phys. Rev. B* **50**, 17953–17979 (1994).
- Togo, A. & Tanaka, I. First principles phonon calculations in materials science. *Scr. Mater.* **108**, 1–5 (2015).
- Grimme, S. et al. A consistent and accurate ab initio parametrization of density functional dispersion correction (DFT-D) for the 94 elements H–Pu. *J. Chem. Phys.* **132**, 154104 (2010).
- Grimme, S., Ehrlich, S. & Goerigk, L. Effect of the damping function in dispersion corrected density functional theory. *J. Comput. Chem.* **32**, 1456–1465 (2011).
- Zhou, Y. et al. Direct synthesis of large-scale WTe₂ thin films with low thermal conductivity. *Adv. Funct. Mater.* **27**, 1605928 (2017).

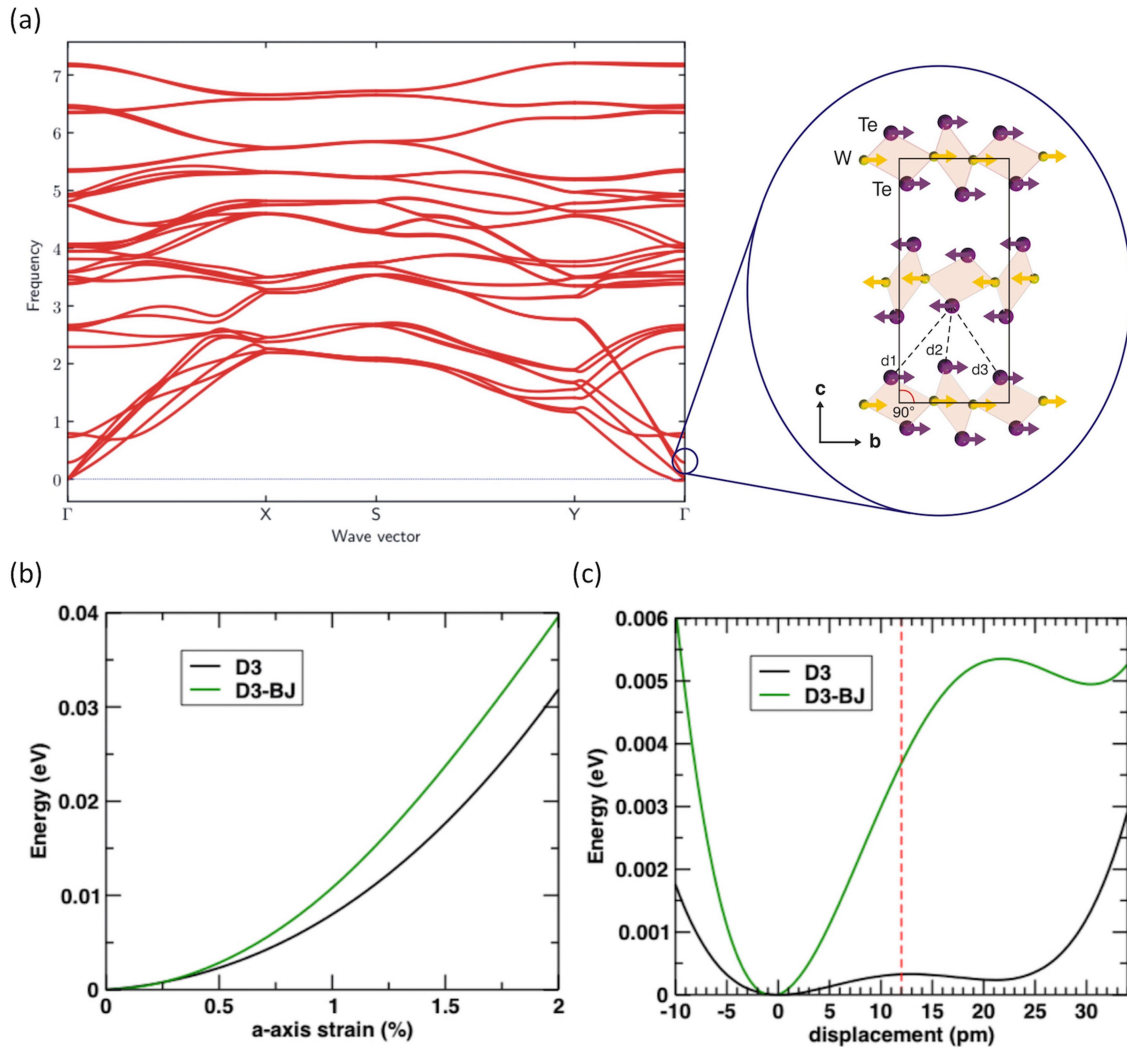


Extended Data Fig. 1 | Lattice structure variants of WTe_2 . **a**, The Td phase has an orthorhombic non-centrosymmetric unit cell with b - c angle of 90° and bond length $d_1 > d_3$. **b**, The $1T'(^*)$ phase has an orthorhombic

centrosymmetric unit cell with a b - c angle of 90° and bond length $d_1 = d_3$. **c**, The $1T'$ phase has a monoclinic centrosymmetric unit cell with a b - c angle of about 94° and bond length $d_1 < d_3$.

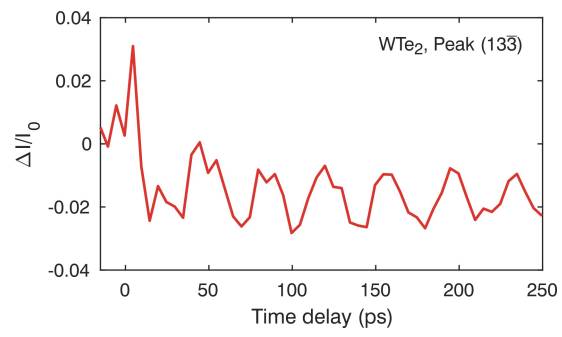


Extended Data Fig. 2 | Electro-optical sampling data of the terahertz pump pulses. **a**, Time trace of terahertz electric field, generated using OH-1 and DSTMS crystals. Curves in **a** are offset for clarity. **b**, Frequency bandwidth of the terahertz field, calculated using the Fourier transform of **a**.

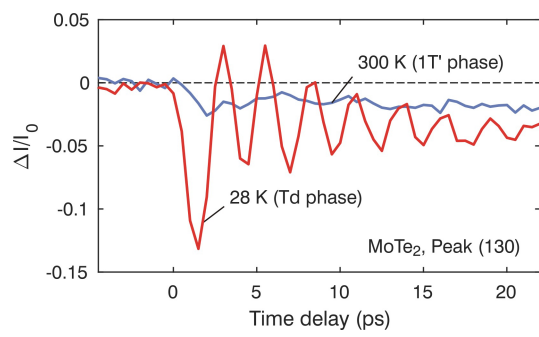


Extended Data Fig. 3 | Calculated phonon dispersion of Td WTe₂ and energy potential as a function of lattice deformation. **a**, Dispersions for wave vectors along high-symmetry lines in the $k_z = 0$ plane are shown. The schematic on the right shows the interlayer shear motion as rigid displacements between alternating WTe₂ layers. **b**, Energy as a function of uniaxial strain applied along the a axis. We used two different forms for the dispersion corrections, namely, DFT-D3 (labelled D3) and DFT D3 with Becke–Johnson damping (labelled D3-BJ). These two corrections

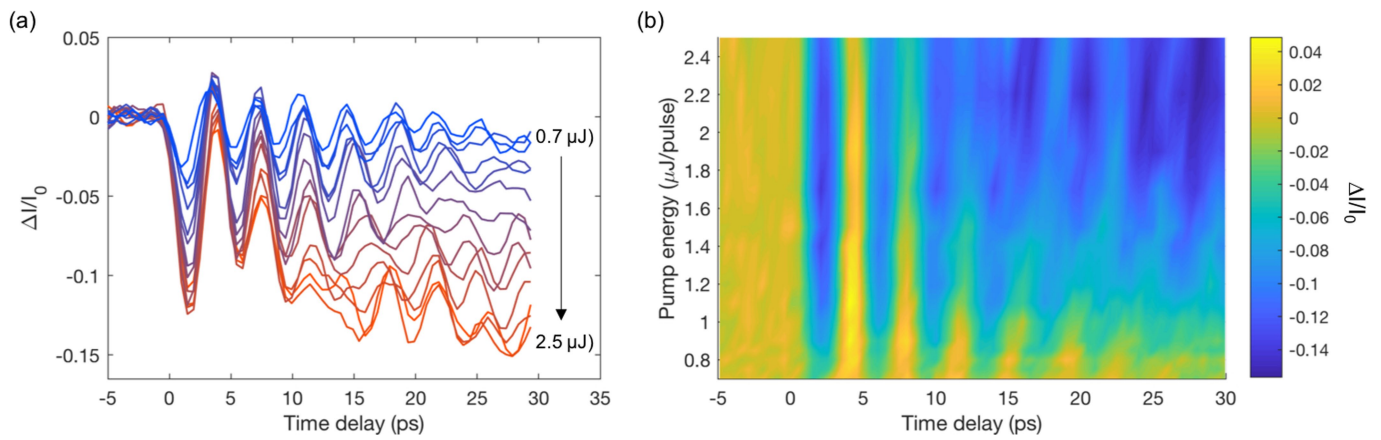
result in slightly different lattice constants, as shown in Extended Data Table 1c, and yield potential energy surfaces that are too shallow and too steep in the D3 and D3-BJ approximations, respectively. The correct description lies between the two limits represented by D3 and D3-BJ. **c**, Energy as a function of displacement along the shear-mode coordinate. The red dashed line indicates the displacement at which two pairs of Weyl nodes annihilate at the $k_y = 0$ mirror plane (see Fig. 4).



Extended Data Fig. 4 | Transverse acoustic propagation dynamics in Td-WTe₂. The structure-factor modulation is monitored using a terahertz-pump UED probe.

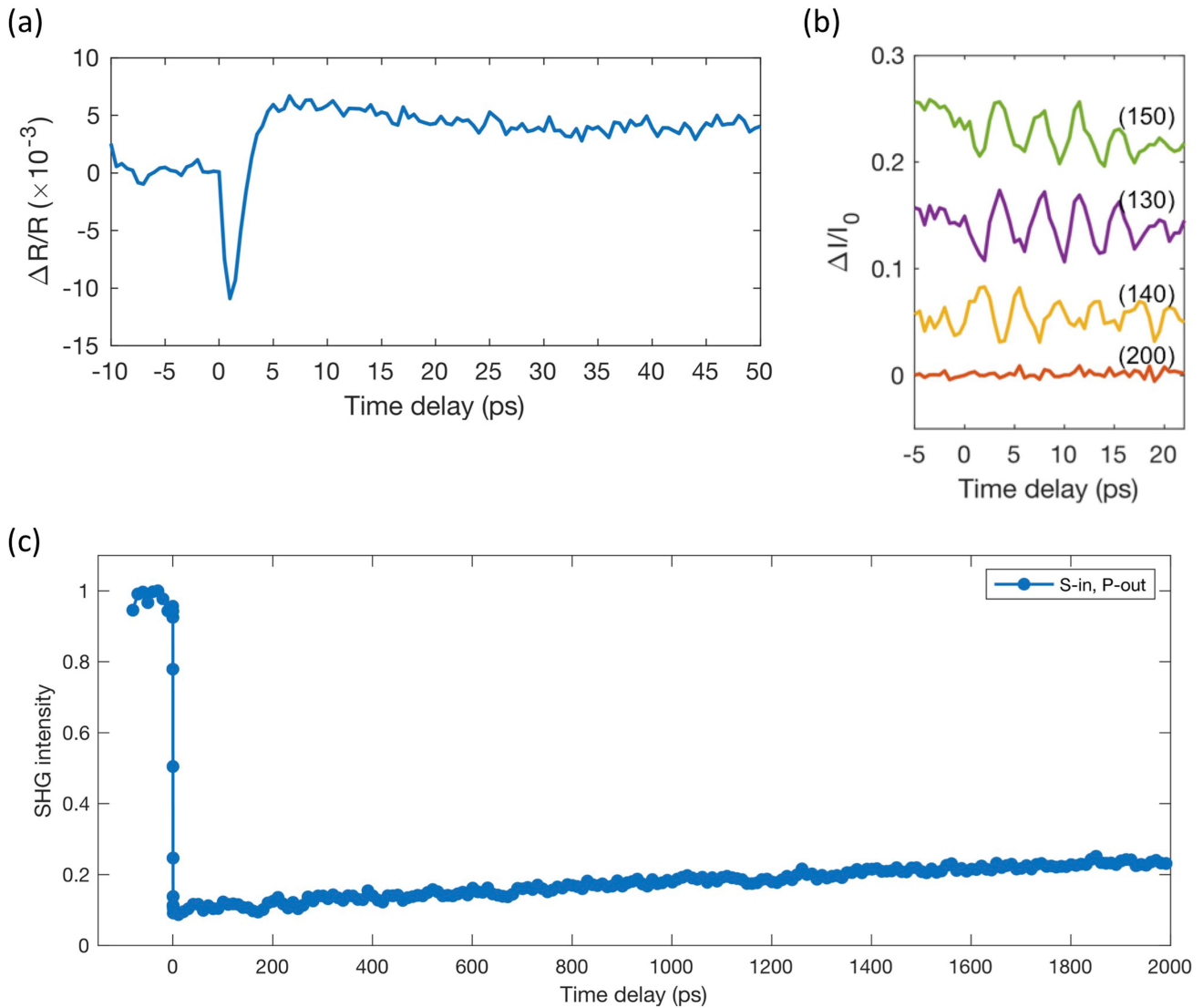


Extended Data Fig. 5 | The emergence of terahertz-induced shear oscillations in Td MoTe₂, but not in 1T' MoTe₂. The structure-factor modulations are monitored using a terahertz-pump UED probe.



Extended Data Fig. 6 | Additional terahertz-pump UED-probe measurements at increasing pump fluence. **a**, Intensity changes of the (130) Bragg peak show the interlayer shear oscillation, which exhibits a phonon softening at larger pump fluences. This demonstrates the

evolution towards switching behaviour in the transition region. **b**, Surface plot of **a**, where $\Delta I/I_0$ is shown by the colour scale. In **b** we use interpolation to show a clearer picture on the frequency shifting at larger pump fluences.



Extended Data Fig. 7 | Optical and structural changes in WTe₂ induced by 2.1- μm pump pulses. **a**, The transient reflectivity of the 800-nm probe gives a direct experimental probe to the electronic system. There is an abrupt change in $\Delta R/R$ right after the pump pulse arrival (within 5 ps). Afterwards, the $\Delta R/R$ signal remains finite and stable for longer than 50 ps. **b**, Bragg peak intensity changes probed by the electron beam. The intensity changes show oscillations that correspond to the interlayer shear-mode frequency of 0.24 THz, similar to the effect produced by the

terahertz pump pulses discussed in the main text. **c**, Time-resolved SHG of WTe₂ at nanosecond time delay. Here, the pump pulse has a wavelength of 2.1 μm (polarized at 45° off the horizontal axis), the incident probe pulse has a wavelength of 800 nm, the crystal *a* axis is aligned horizontally and the SHG is detected at the 'S-in, P-out' configuration. This shows that the light-induced centrosymmetric phase lives for a few nanoseconds, or even tens of nanoseconds, which is consistent with the induced metastable phase discussed in the main text.

Extended Data Table 1 | Lattice and electronic structure parameters for DFT calculations

(a)

	W(1)	W(2)	Te(1)	Te(2)	Te(3)	Te(4)
y	0.60062	0.03980	0.85761	0.64631	0.29845	0.20722
z	0.5	0.01522	0.65525	0.11112	0.85983	0.40387

(b)

	k_x	k_y	k_z	C
WP1	0.12195	0.03947	0	+1
WP2	0.12160	0.04510	0	-1

(c)

	a (Å)	b (Å)	c (Å)	d_1 (Å)	d_2 (Å)	d_3 (Å)	ν_{shear} (THz)
D3	3.4807	6.2806	13.9973	5.3104	3.8734	5.0137	0.15
D3-BJ	3.4841	6.2528	13.5910	5.2570	3.7169	4.7787	0.34
Experiment [5]	3.477	6.249	14.018	5.397	3.911	4.937	0.24

a, Wyckoff position parameters for the coordinates of two W and four Te atoms in the experimentally determined unit cell of WTe_2 ^{16,42}. **b**, Coordinates of the two WPs that occur in the first quadrant of the $k_z = 0$ plane of the BZ of WTe_2 . The last column indicates the Chern number (C) of the nodes. **c**, Calculated lattice and interlayer distance parameters of Td WTe_2 compared to experimental values. The last column shows the calculated phonon frequency (ν_{shear}) of the b -axis shear mode of interest. This table has been reproduced from ref. ¹⁶, Springer Nature.